Check for updates

Healing of donor defect states in monolayer molybdenum disulfide using oxygen-incorporated chemical vapour deposition

Pin-Chun Shen [1,8], Yuxuan Lin [1,8], Cong Su [2], Christina McGahan [3], Ang-Yu Lu[1], Xiang Ji[1], Xingzhi Wang [4], Haozhe Wang [1], Nannan Mao[1,5], Yunfan Guo[1], Ji-Hoon Park [1], Yan Wang[6], William Tisdale [5], Ju Li [2], Xi Ling [4,7], Katherine E. Aidala[3], Tomás Palacios [1] and Jing Kong [1✉]

Two-dimensional molybdenum disulfide (MoS₂) is a semiconductor that could be used to build scaled transistors and other advanced electronic and optoelectronic devices. However, the material typically exhibits strong n-type doping, low photoluminescence quantum yields and high contact resistance with metals, behaviour that is often attributed to the presence of donor states induced by sulfur vacancies. Here we show that oxygen-incorporated chemical vapour deposition can be used to passivate sulfur vacancies and suppress the formation of donor states in monolayer MoS₂. First-principles calculations and spectroscopy measurements are used to reveal the formation of molybdenum–oxygen bonding at the sulfur vacancy sites and the absence of donor states in oxygen-incorporated MoS₂. Compared with MoS₂ fabricated via chemical vapour deposition without oxygen, oxygen-incorporated MoS₂ exhibits enhanced photoluminescence, higher work function and improved contact resistance with a lower Schottky barrier (less than 40 meV) at the metal/MoS₂ interface.

The semiconductor industry relies on engineering the electronic and optical properties of semiconductor crystals—without degrading performance—using techniques such as doping[1], stoichiometry[2], defect engineering[3] and interfacial effects[4]. Transition metal dichalcogenides (TMDs), such as monolayer molybdenum disulfide (MoS₂), has been proposed as an alternative semiconductor to silicon due to their bandgap (1.8−1.9 eV), moderate carrier mobility and atomically thin body (6.5 Å), which is ideal for gate electrostatic control and device downscaling[5]. However, the thinness of TMD monolayers also makes them highly susceptible to intrinsic and extrinsic defects and impurities[6,7]. It has, in particular, been theoretically predicted and experimentally observed that the electron transport and excitonic transitions of MoS₂ are strongly affected by defects[7,8], strain[9] and substrate effects[10].

Sulfur vacancies (V_S) are the most commonly observed natural structural defects in MoS₂ due to their lower formation energy compared with other structural defects[11,12], and typical densities of V_S in monolayer MoS₂ can be up to 10^{13} cm^{-2} (ref. [13]). These vacancies induce defect states localized below the conduction band minimum (CBM) of MoS₂ (refs. [14,15]) and can be detrimental to the performance of electronic and optoelectronic devices, acting as scattering centres that limit carrier mobility[7,8], and mediating non-radiative recombinations that reduce the photoluminescence (PL) efficiency[16,17]. In addition, V_S can function as electron donors due to unsaturated bonds, resulting in strong electron (n-type) doping in monolayer MoS₂ (ref. [18]). As a result, PL intensity is decreased due to quenching of the optical transitions of neutral excitons and formation of charged exciions (trions) in electron-rich environments[17,19]. When in contact with metals, V_S-induced defect states in the bandgap cause Fermi-level pinning, resulting in high Schottky barriers[14,20–22]. The Schottky barrier height (SBH) at metal/MoS₂ interfaces is typically in the range of 100−400 meV (refs. [22–27]), which impedes electronic transport and results in poor electrical contact resistance (R_C). Thus, to improve the performance of MoS₂-based electronic and optoelectronic devices, approaches to passivate the V_S in the material are required.

Doping and defect engineering in MoS₂ are, however, challenging due to its low dimensionality. The V_S can be physically passivated through surface modification, such as superacid treatment[16], thiol chemistry modification[28] and oxygen physio-adsorption[29,30]. These physical treatment methods can repair the V_S and reduce the density of trap states, thus enhancing the exciton emission efficiency and electron mobility in MoS₂. Though surface modifications by molecules and ions can locally alter the electronic and optoelectronic properties, these treatments suffer from chemical instability and incompatibility with device fabrication processes. Several chemical treatment approaches have also been developed, such as high-temperature annealing in a sulfur-rich or oxygen-rich environment[30,31], laser-irradiation-assisted oxygen adsorption[32], and ion radiation and plasma treatment[33–35]. These methods are more stable than surface modification, but crystallinity and uniformity are inevitably compromised.

In this Article, we report a scalable oxygen-incorporated chemical vapour deposition (O₂-CVD) technique that can suppress the formation of donor defect states in monolayer MoS₂. Using density functional theory (DFT) calculations, the presence of oxygen at the V_S sites is shown to passivate the V_S-induced donor energy levels and reduce undesired n-type doping, as well as preserving

¹Department of Electrical Engineering and Computer Science, Massachusetts Institute of Technology, Cambridge, MA, USA. ²Department of Nuclear Science and Engineering, Massachusetts Institute of Technology, Cambridge, MA, USA. ³Department of Physics, Mount Holyoke College, South Hadley, MA, USA. ⁴Department of Chemistry, Boston University, Boston, MA, USA. ⁵Department of Chemical Engineering, Massachusetts Institute of Technology, Cambridge, MA, USA. ⁶Institute of Microelectronics, Tsinghua University, Beijing, China. ⁷Division of Materials Science and Engineering, Boston University, Boston, MA, USA. ⁸These authors contributed equally: Pin-Chun Shen, Yuxuan Lin. ✉e-mail: jingkong@mit.edu

the electronic band structure and carrier mobility. Electron depletion of the passivated MoS_2 is confirmed by Raman, PL, X-ray photoelectron spectroscopy (XPS) and electrostatic force microscopy (EFM), as well as by the shift in the threshold voltage of MoS_2 transistors. We also show enhanced PL emissions due to reduced non-radiative recombinations and electron depletion, reduction in Schottky barrier (<40 meV) and improvement in contact resistance at the metal/MoS_2 interface (1 kΩ μm), which is due to suppression of the defect-induced Fermi-level pinning effect. Gate-dependent PL measurements at low temperature show an absence of donor-defect-bound excitons in the oxygen-incorporated MoS_2, compared with CVD-grown MoS_2 without oxygen incorporation.

Deposition of monolayer MoS_2 with oxygen

To study the effects of oxygen in the growth environment on the performance of MoS_2, three conditions are designed and used to obtain three distinct types of monolayer MoS_2 crystal, namely, oxygen-incorporated MoS_2 (O-MoS_2), MoS_2 grown under the sulfur-mild condition (SM-MoS_2) and MoS_2 grown under the sulfur-excess condition (SE-MoS_2). Typical optical microscopy images are shown in Fig. 1a–c. These three types of MoS_2 crystal are deposited on 300 nm SiO_2/Si substrates at 625 °C for 3 min through the sulfurization of molybdenum trioxide (MoO_3) powder using our previously reported perylene-3,4,9,10-tetracarboxylic acid tetrapotassium (PTAS)-molecules-assisted CVD method[36]. Besides the carrier gas of Ar, an additional flow of oxygen gas is introduced during deposition to provide the oxygen source. The experimental CVD setup and detailed growth conditions are provided in Supplementary Section 1. For typical CVD of MoS_2 grown without oxygen, triangular shapes are dominantly present at the optimized sulfur-mild condition (SM-MoS_2; Fig. 1a) (O_2, 0 s.c.c.m.; S, 20 mg; MoO_3, 20 mg), whereas a sulfur-rich condition (O_2, 0 s.c.c.m.; S, 40 mg; MoO_3, 20 mg) yields concave MoS_2 crystals whose edges are inwardly curved (SE-MoS_2; Fig. 1b), reflecting the mismatch of the growth rate at the crystal edges owing to the highly unbalanced precursor ratio during the growth[37]. These two flake types represent the most common MoS_2 crystals obtained through CVD methods[7,36,38–41].

According to the Mo–O–S ternary phase diagram (Fig. 1e), the presence of moderate amounts of oxygen in the O_2-CVD system could offer a chemical path to obtain partially oxidized MoS_2 (referred to as O-MoS_2 in this work). Additionally, PTAS-assisted CVD allows the growth of O-MoS_2 crystals at a lower temperature with a shorter deposition time[36], which avoids the anisotropic oxidative etching of MoS_2 previously reported (850 °C, >30 min)[42]. We note that the presence of oxygen tends to shape the crystals into a convex geometry (Fig. 1c; O_2, 0.2 s.c.c.m.; S, 20 mg; MoO_3, 20 mg), which has not been revealed in a previous study[42], indicating a different growth regime in our study. Supplementary Fig. 2 shows that the crystal geometries undergo a clear evolution from triangular to hexagonal and then to circular as the flow rate of oxygen increases. Within our proposed process windows, no etching effects on the as-grown crystals are observed. Previous theoretical work has shown that these convex crystal geometries are more energetically favourable in a sulfur-deficient growth condition because the formation energies of various edge configurations such as Mo zigzag edge, S zigzag edge and armchair can be nearly equivalent in such a growth environment, whereas S zigzag edges have less formation energies in a sulfur-rich environment, resulting in a triangular shape[43]. A thickness below 1 nm characterized by atomic force microscopy confirms that the as-grown O-MoS_2 crystals are monolayer (Supplementary Fig. 3d). Second-harmonic generation measurements reveal that the individual O-MoS_2 domain is single crystalline without grain boundaries (Supplementary Section 2 provides further details)[44]. To clarify the structure of monolayer O-MoS_2, transmission electron microscopy (TEM) characterization is carried out (Fig. 1f,g). The

selected-area electron diffraction pattern for the as-grown monolayer O-MoS_2 (Fig. 1g) shows a set of sixfold-symmetric diffraction points, corresponding to the monolayer hexagonal lattice structure of MoS_2 (ref. [39]). In addition to O-MoS_2, layered MoO_2 can also be formed when a high flow rate of oxygen (O_2, 2 s.c.c.m.; S, 20 mg; MoO_3, 20 mg) is introduced (Fig. 1d). The lack of gate dependence and high conductivity shown in Supplementary Fig. 4b,c reveal the metallic nature of these CVD-grown layered MoO_2 crystals.

XPS measurements confirm the presence of Mo–O bonds and less n-type doping in the as-grown O-MoS_2. The peak located at 530.3 eV in the O 1s spectra as well as the two well-pronounced MoO_x-related peaks at 232.3 and 235.4 eV for Mo(VI) $3d_{5/2}$ and Mo(VI) $3d_{3/2}$ in the Mo 3d spectra[30,45,46] (Fig. 1h,i), respectively, signify the existence of covalent Mo–O bonds in the O-MoS_2 sample. These Mo–O bonds may originate from either oxygen-passivated sulfur vacancies in MoS_2 or residual clusters of MoO_x during growth; therefore, before XPS characterization, the O-MoS_2 sample is carefully rinsed by deionized water and isopropyl alcohol to remove MoO_x on the surface. Importantly, the XPS data of O-MoS_2 exhibit a redshift in binding energies for both Mo(IV) $3d_{5/2}$ from 229.7 to 229.4 eV and S 2s from 226.7 to 226.4 eV (Fig. 1h). Similar shifts are also observed for the S2p peaks (Supplementary Fig. 8). The binding-energy redshifts can be translated to a downward shift of 0.3 eV of the Fermi level in O-MoS_2, that is, the Fermi level moves towards the valence band maximum, indicating less n-type doping[47]. These observations suggest the electron depletion of the as-grown monolayer O-MoS_2 crystals as compared with regular CVD MoS_2 crystals.

Reduction in n-type doping of O-MoS_2

The first effect of oxygen on the as-grown O-MoS_2 crystals is PL enhancement. Figure 2a compares the room-temperature PL spectra of three types of monolayer MoS_2. The distinct PL peaks at 1.8–1.9 eV and the absence of indirect emission peaks at lower energies confirm that the as-grown MoS_2 crystals are monolayer[48]. Similar to previous studies on surface-defect-passivation treatment[16], p-type chemical doping[19] or electrostatic hole doping[17] of MoS_2, the O-MoS_2 crystals also exhibit an enhanced PL with a higher peak energy of 1.87 eV. In contrast, the PL intensity decreases and PL peak shifts towards a lower energy with an increased amount of sulfur involved during the growth (1.85 and 1.83 eV for SM-MoS_2 and SE-MoS_2, respectively). The PL of MoS_2 at room temperature is mainly attributed to the radiative optical transitions of neutral excitons and trions and is highly sensitive to doping and impurities[17,19,48]. The blueshift in the PL peak in O-MoS_2 suggests that the neutral excitons are much more populated than trions in the crystals[17,19], a common sign of less n-type doping and fewer defect states. This also results in the suppression of non-radiative recombination and enhanced PL intensity. The emission energy difference between O-MoS_2 and SM- or SE-MoS_2 samples can be observed more clearly on the PL mapping results, where the O-MoS_2 flake (Fig. 2a,c) has a PL emission energy of 1.87 eV, corresponding to neutral A-exciton emission[48], whereas both SM-MoS_2 and SE-MoS_2 crystals exhibit lower PL emission energies at around 1.84 and 1.82 eV, respectively (Fig. 2a,d,e), indicating their trion-dominated characteristics.

Raman spectroscopy is carried out to quantitatively characterize the doping concentration. The distributions of doping concentration and strain can be simultaneously extracted from the Raman shifts of the two vibrational modes (Supplementary Section 4)[10,49,50]. As shown in Fig. 2b, the as-grown O-MoS_2 exhibits a blueshift in the A_{1g} vibrational mode as opposed to those in both SM-MoS_2 and SE-MoS_2, which can be translated into a lower electron concentration[10,51]. The spatial distributions of change in electron concentrations extracted from the Raman shifts are shown in Fig. 2f–h. For the MoS_2 crystals grown in typical CVD environments without oxygen (namely, SM-MoS_2 and SE-MoS_2), high levels of n-type doping
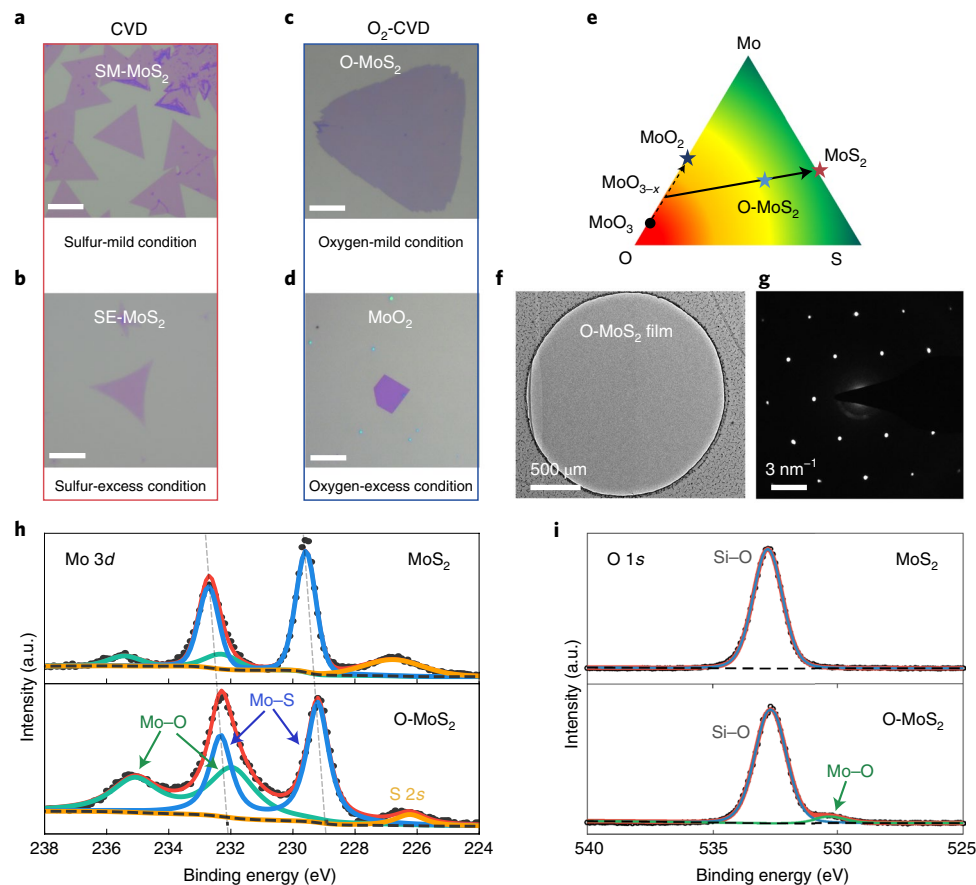
Fig. 1 | Deposition of monolayer MoS₂ with and without oxygen incorporation. a, Optical image of a typical monolayer MoS₂ crystal grown without oxygen under the sulfur-mild condition, showing a triangular shape. **b**, Optical image of a monolayer MoS₂ crystal grown without oxygen under a sulfur-excess condition. The crystal shows inward curved edges (concave shape). **c**, Optical image of a monolayer MoS₂ grown in an oxygen-mild environment. The crystal shows outward curved edges (convex shape). **d**, Optical image of a metallic layered MoO₂ flake obtained at a high flow rate of oxygen. Scale bars, 10 μm (**a–d**). **e**, Ternary phase diagram of MoS₂, indicating the possible reaction routes for CVD growth of MoS₂. The star symbols represent the products obtained in this work. **f**, A TEM image of O-MoS₂. **g**, A selected-area electron diffraction pattern of the monolayer O-MoS₂ film. The sixfold-symmetric diffraction points correspond to the hexagonal lattice structure of monolayer MoS₂, indicating the highly crystalline nature of the as-grown crystals. **h,i**, XPS data of Mo 3d (**h**) and O 1s (**i**) for a typical CVD MoS₂ film grown under the sulfur-mild condition and an O-MoS₂ film, showing the presence of Mo–O bonds in O-MoS₂. The dashed lines highlight the shift in binding energies. The redshifted binding energies in the O-MoS₂ film indicate the less n-type doping in O-MoS₂. The weak intensity of Mo–O peaks in a typical CVD MoS₂ film is likely to be associated with the physisorption of oxygen in the environment[30] or MoO$_x$ clusters deposited onto the substrate during the growth.

are observed, which is consistent with previously reports results[10]. In contrast, this unintentional n-type doping is substantially suppressed in the O-MoS₂ sample. This observation is also consistent with the trend found in the PL spectra. A detailed discussion on the strain distributions in these three types of as-grown MoS₂ crystal and its effects on PL are provided in Supplementary Section 4.

DFT calculations are performed to understand the effects of V_S and oxygen dopants on the monolayer MoS₂ samples. Figure 3 shows the atomic structures and local density of states (LDOS) of defective and oxygen-incorporated monolayer MoS₂. Compared with perfect monolayer MoS₂ (Fig. 3a), the presence of V_S introduces donor defect states within the bandgap of MoS₂ (Fig. 3b). These states increase the electron concentrations and decrease the work function of MoS₂ (Supplementary Fig. 11a). On the other hand, when the V_S sites are bound to one or two oxygen atoms, such donor defect states are eliminated, giving rise to the depletion of electrons and an increased work function in O-MoS₂ (Fig. 3c,d and Supplementary Fig. 11b). This theoretical observation agrees with previous experimental results[52] and can explain the electron depletion effect discussed above, as well as the transport properties of

O-MoS₂ transistors (discussed later). There are additional features in the DFT calculation results that are related to the low-temperature spectroscopic characteristics induced by oxygen passivation, which will also be discussed later.

Improved performance of monolayer O-MoS₂ transistors

The removal of the donor state in O-MoS₂ crystals can greatly alter the device performance. We fabricate field-effect transistors (FETs) based on three types of MoS₂ sample (Fig. 4a) and characterize the transport properties. The electrical characterization of transistors is conducted in a high-vacuum environment (~10⁻⁶ torr) to avert other extrinsic doping effects induced by air or moisture. As evident in Fig. 4b, a clear shift in the threshold voltage (V_T) is observed in the O-MoS₂ FET with respect to the other two samples, which suggests lighter n-type doping in the O-MoS₂ channel. A statistical analysis of V_T shifts and field-effect mobilities (μ) for these three types of MoS₂ FET is shown in Fig. 4b, inset, and Supplementary Fig. 15. The V_T values for the SE-MoS₂ and SM-MoS₂ transistors lie in -17.0 ± 9.7 V and 2.8 ± 4.9 V, respectively, whereas the transistors based on the electron-depleted O-MoS₂ monolayers exhibit a 'normally
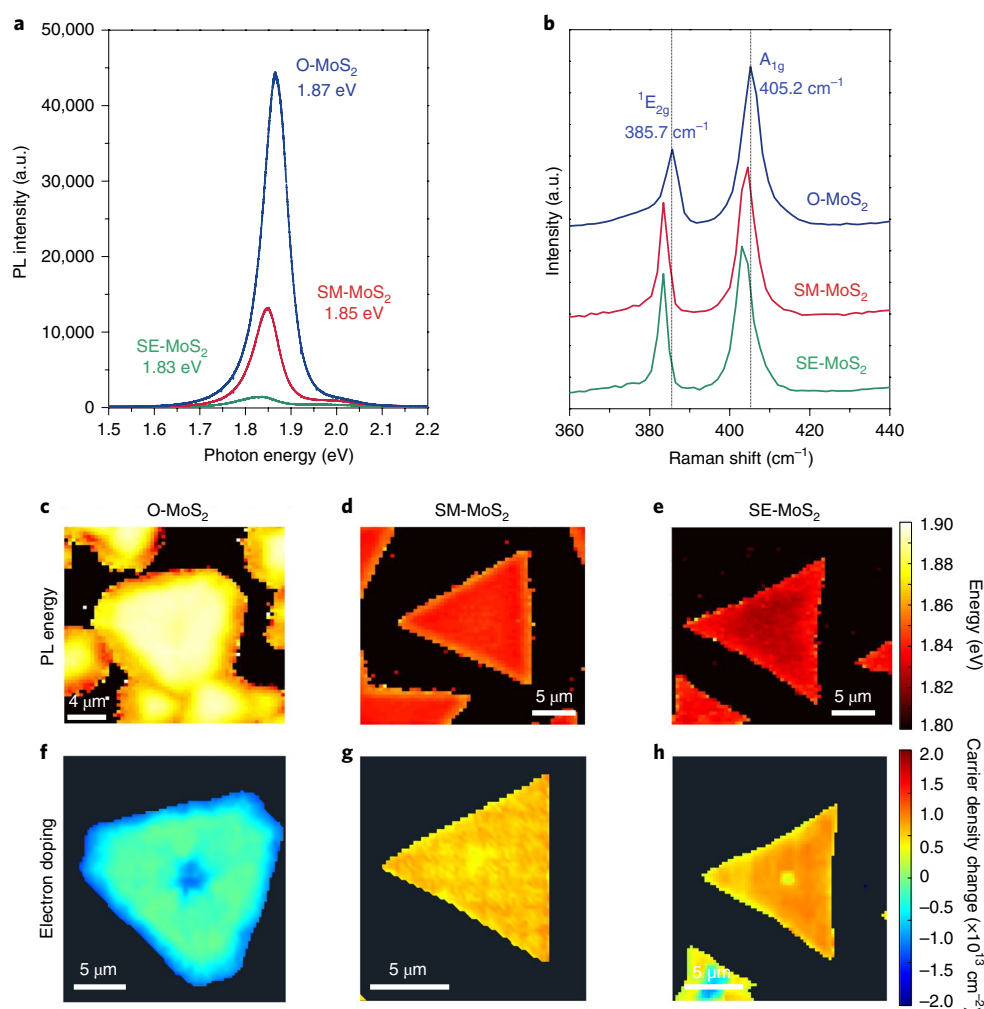
Fig. 2 | Reduction in electron doping of monolayer O-MoS₂. a, Typical PL spectra of O-MoS$_2$, SM-MoS$_2$ and SE-MoS$_2$ flakes grown on SiO$_2$/Si substrates acquired in an ambient environment, showing PL enhancement of O-MoS$_2$. **b**, Typical Raman spectra taken from these three types of MoS$_2$ monolayer. The blueshift in A$_{1g}$ for O-MoS$_2$ suggests lower electron doping. **c–e**, Mapping of PL energy for the three types of MoS$_2$ flake. The electron-depleted domain of O-MoS$_2$ (**c**) shows a PL peak energy close to the neutral excitonic transition. In contrast, SM-MoS$_2$ (**d**) and SE-MoS$_2$ (**e**) crystals grown without oxygen display lower PL energies, corresponding to charged exciton (trion) transition. **f–h**, Mapping of the change in carrier densities extracted from the A$_{1g}$ shifts for O-MoS$_2$ (**f**), SM-MoS$_2$ (**g**) and SE-MoS$_2$ (**h**). A significant reduction in electron doping is observed in O-MoS$_2$.

off' characteristic with a positive V_T of 21.0 ± 4.6 V. The V_T difference among these three types of transistor can be attributed to the Fermi-level shift in the MoS$_2$ channels, which are in accordance with the doping concentration difference observed in the PL and Raman measurements and the work-function shifts from DFT calculations. No mobility degradation is observed in the O-MoS$_2$ samples. The electrical characteristics and PL spectra of O-MoS$_2$ are consistent in both vacuum and air (Supplementary Figs. 25 and 26), suggesting the stable chemical bonding, rather than physisorption, of the oxygen dopants to the MoS$_2$ lattice.

The work functions of monolayer MoS$_2$ FET channels with and without oxygen incorporation are experimentally characterized via EFM. The insets in Fig. 4c show the scans of the EFM phase of MoS$_2$ (top-left inset) relative to the grounded Au electrode (bottom-right inset) for the same tip voltage. The striking phase contrast difference between O-MoS$_2$ (top) and SM-MoS$_2$ (bottom) suggests a difference in their electrical properties, and their work functions extracted from a series of EFM scans at different tip voltages are shown in Fig. 4c (Supplementary Fig. 9b). More details about the extraction of work function from EFM is provided in Supplementary Section 6. Figure 4c demonstrates that O-MoS$_2$ indeed exhibits a

higher work function than SM-MoS$_2$. This increase in work function with oxygen incorporation is consistent with experimental observations from PL, Raman and electrical characterization. Taking the work function of Au electrodes as the reference (5.2 eV)[22], O-MoS$_2$ has a work function of 5.45 ± 0.05 eV, which is higher than the reported values for MoS$_2$ treated with physically absorbed oxygen and plasma-treated MoS$_2$ (ref. [34,53]). This work function is also distinct from that of SM-MoS$_2$, which is 5.19 ± 0.05 eV. These results are in good agreement with the DFT calculations (Fig. 4c and Supplementary Fig. 11).

The incorporation of oxygen into monolayer O-MoS$_2$ also reduces the contact resistance of MoS$_2$ devices. Figure 4d and Supplementary Fig. 12 show the room-temperature output characteristics (I_{DS}–V_{DS}) of three types of monolayer MoS$_2$ transistor with Ni contacts. The O-MoS$_2$ FETs exhibit ohmic-like characteristics at room temperature, whereas the SM-MoS$_2$ and SE-MoS$_2$ transistors show nonlinear, Schottky characteristics. This linear I_{DS}–V_{DS} response for the O-MoS$_2$ transistors suggests that the energy barrier at the Ni/O-MoS$_2$ interface is relatively small. To investigate the energy barrier at the contact interface, the thermionic emission model is applied to extract the Schottky barriers at the
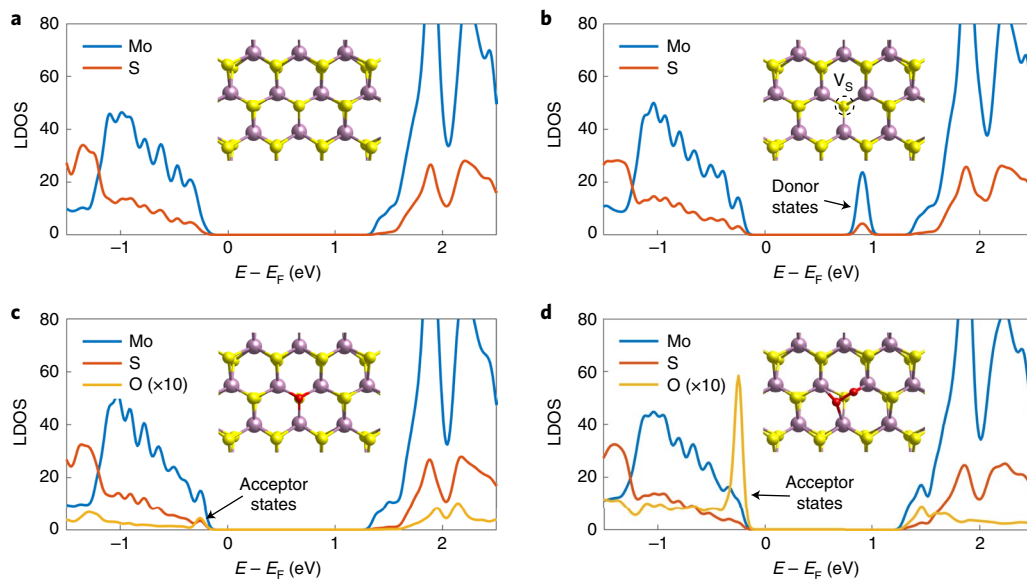
Fig. 3 | Atomic structures and DFT calculation results of the effect of oxygen healing. a, LDOS as a function of the electron energy (E) relative to the Fermi level E_F of pristine monolayer MoS_2. Inset: atomic structure of monolayer MoS_2 (purple, molybdenum atoms; yellow, sulfur atoms). **b**, LDOS of defective monolayer MoS_2 possessing V_S. Donor-like states emerge below the conduction band edge. The V_S site is highlighted by the dashed circle shown in the inset. **c,d**, LDOS of monolayer MoS_2 with a single oxygen atom (red atom in the inset) (**c**) and two oxygen atoms (red atoms in the inset) (**d**) bonded to the V_S sites. The presence of oxygen dopants heals the V_S-induced donor defect states and introduces additional acceptor-like states near the valence band edges. Insets, corresponding atomic structures obtained from the DFT calculations.

Ni/MoS_2 junction (Supplementary Section 10). Supplementary Fig. 17 shows the extracted effective energy barriers at various gate voltages for these three types of transistor. The SBH in the O-MoS_2 FET at the flat-band condition is extracted to be 40 meV (Supplementary Fig. 17d), which are much lower than those extracted from both SE-MoS_2 and SM-MoS_2 devices (namely, 100 and 200 meV, respectively; Supplementary Fig. 17e,f). Such a low contact barrier is confirmed in several O-MoS_2 FETs (Supplementary Fig. 18). Note that the SBH observed in O-MoS_2 FET is also smaller than those characterized from different types of contact to MoS_2 devices in previous reports (100–400 meV)[22–27]. For a high-SBH device such as SE-MoS_2 and SM-MoS_2 FETs, the drain current (I_{DS}) significantly drops with decreasing temperature, which is due to the reduced thermionic emission current across the Schottky barrier (Supplementary Fig. 14b,c). We note that I_{DS} in the O-MoS_2 FET shows lower sensitivity to the decrease in temperature (Supplementary Fig. 14a), reflecting the nature of the lower energy barrier at the contact interface, although its I_{DS}–V_{DS} curves still turn to nonlinear characteristics at a low temperature due to the presence of the small Schottky barrier (Supplementary Fig. 13).

Given that SBH is supposed to be equal to the energy difference between the work function of the metal contact and the electron affinity of the semiconductor in an ideal case (Schottky–Mott limit), such inconsistency in SBHs for these three types of FET implies the presence of different extents of Fermi-level pinning at the Ni/MoS_2 interfaces (Fig. 4g–j). There are two possible origins of Fermi-level pinning: pinning by metal-induced gap states (MIGS)[54], in which the electron wave functions of the metal 'leak' into the semiconductor at the interface, resulting in a broad continuum of states in the bandgap of the semiconductor, and giving rise to Fermi-level pinning somewhere within the bandgap; in defect-state pinning, the Fermi level is pinned at the energy level with the highest density of defect states[55,56]. Neither of these two pinning mechanisms is necessarily correlated with the energy difference between metal work function and electron affinity of the semiconductor. Generally speaking, these two pinning mechanisms compete at the

metal/semiconductor interface, and the Fermi level is fixed at the overall charge neutrality level. Given the abundant V_S states below the CBM in SM- or SE-MoS_2, and the absence of any deep donor states in O-MoS_2 as predicted by the DFT calculation results (Fig. 3 and Supplementary Fig. 10), we believe that the SBHs in SM- or SE-MoS_2 and in O-MoS_2 are dominated by defect-state pinning and MIGS pinning, respectively, in which the Fermi level determined by MIGS may be closer to the CBM of MoS_2, allowing for a lower SBH.

The R_C value for a semiconductor device is determined by the SBH at the interface. We extract the R_C value of the three types of MoS_2 FET through the transfer length method[26,57]. As expected, SM-MoS_2 and SE-MoS_2 FETs exhibit high R_C of around 3.9 and 7.8 kΩ μm, respectively, due to their high SBHs (Fig. 4e and Supplementary Fig. 19b). Compared with typical CVD MoS_2 grown without oxygen, the low SBH of the O-MoS_2 transistor yields a lower R_C value of ~1 kΩ μm at the same carrier density (n_{2D}) of 4×10^{12} cm^{-2} (Fig. 4e and Supplementary Fig. 19b,c). Figure 4e summarizes the resulting SBH and R_C for the three types of monolayer MoS_2 FET. It is worth mentioning that the improved R_C value for the O-MoS_2 FETs is also lower than previously reported Ni[57,58], van der Waals and interlayer contacts ($R_C \approx 3$ kΩ μm)[26,59], as summarized in Fig. 4f.

The monolayer O-MoS_2 FETs exhibit an average field-effect electron mobility of ~15 cm^2 V^{-1} s^{-1} (Fig. 4b, inset), comparable to those in typical CVD MoS_2 in this work and in previous studies[38,41]. This suggests that oxygen incorporation in MoS_2 lattices does not lead to severe mobility degradation caused by either dopant scattering or changes in carrier effective mass (that is, the curvature of CBM of O-MoS_2 is nearly unchanged; Supplementary Fig. 10). It is worth mentioning that although O-MoS_2 monolayers possess an increased work function, the devices still show n-type conduction. This is because Ni contacts used in this study still yield a lower SBH for electron injection (Fig. 4g,i), but rather higher SBH for holes, even after oxygen passivation. One should note that to realize high-performance p-type MoS_2 FETs, two factors must be simultaneously satisfied: first, a channel with a high work function; second, a low SBH at the metal/MoS_2 interface for hole injection. Our results
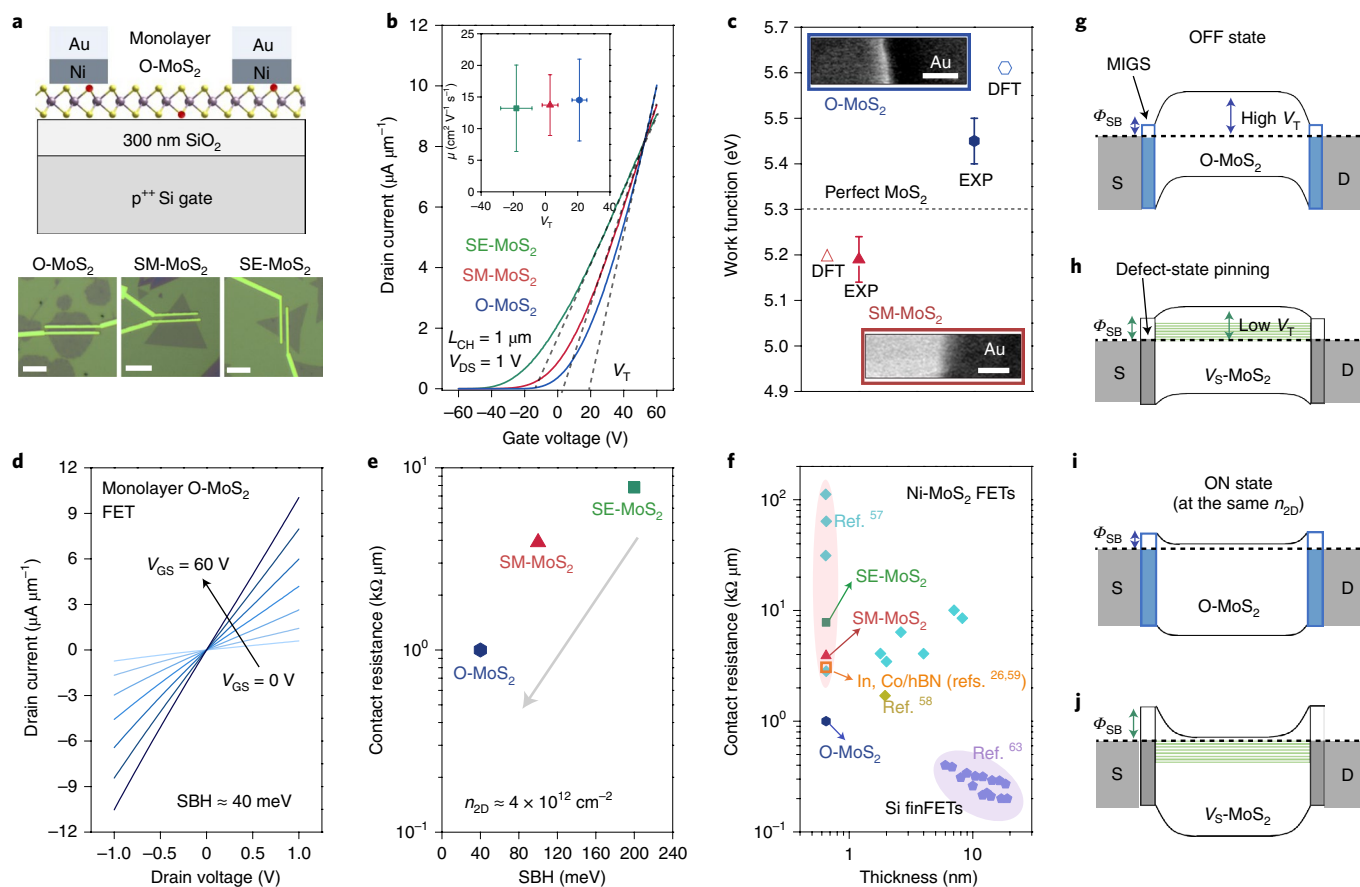
Fig. 4 | Electrical characterization of monolayer O-MoS$_2$ FETs. a, Schematic and the corresponding optical images of as-fabricated FETs with monolayer O-MoS$_2$, SM-MoS$_2$ and SE-MoS$_2$. The channel length (L_{CH}) is 1 μm. Scale bars, 10 μm. **b**, Transfer characteristics (drain current I_{DS} versus gate voltage V_{GS}) at a drain–source voltage (V_{DS}) of 1 V at room temperature. Inset: means and standard deviations of V_T and field-effect mobility (μ) extracted from the measurements of 80 FETs. **c**, Work functions (means and standard deviations) of MoS$_2$ FET channels with and without oxygen incorporation directly measured via EFM (EXP) in a nitrogen environment, as well as those calculated from DFT. Insets: the EFM phase of the monolayer MoS$_2$ (left) channel relative to the grounded Au electrode (right) for the same tip voltage (red, SM-MoS$_2$; blue, O-MoS$_2$; scale bars, 100 nm). The filled hexagon (filled and open triangles) represent the work functions of O-MoS$_2$ (SM-MoS$_2$) acquired from experimental EFM and theoretical DFT, respectively. **d**, Output characteristics (I_{DS} versus drain voltage V_{DS}) of a monolayer O-MoS$_2$ transistor. **e**, R_C versus SBH. The R_C values are extracted at n_{2D} of 4×10^{12} cm^{-2}. **f**, R_C versus thickness of MoS$_2$ transistors with Ni contacts (light blue and yellow) and van der Waals contacts (orange) and one example of Si fin field-effect transistors (finFETs; purple) from the literature[26,57–59,63]. The O-MoS$_2$ monolayers exhibit an improved R_C for Ni-contacted MoS$_2$ FETs. **g,h**, Band diagrams for the OFF states of 2D FETs fabricated on O-MoS$_2$ (**g**) and MoS$_2$ with donor defect states (**h**) (V_S-MoS$_2$ representing both SE-MoS$_2$ and SM-MoS$_2$). S, source; D, drain. Φ_{SB}, Schottky barrier height. The larger work function (namely, the lower Fermi level) of the O-MoS$_2$ channel gives rise to a positive shift of V_T. The MIGS induced at the Ni/MoS$_2$ interfaces are qualitatively illustrated in blue. The presence of the deep donor states (illustrated in green) in defective MoS$_2$ leads to defect-state pinning at the interface, resulting in a higher SBH. **i,j**, Band diagrams for the ON states of the 2D FETs fabricated on O-MoS$_2$ (**i**) and defective MoS$_2$ (**j**) at the same carrier density of the 2D channel, indicating a lower SBH in O-MoS$_2$ FETs.

illustrate the feasibility of enlarging the work function and eliminating the defect-state pinning of the MoS$_2$ channel through a one-step CVD process. Further investigation on various metal contacts to monolayer O-MoS$_2$ would be a promising direction for the development of p-type monolayer MoS$_2$ FETs.

Defect-state-bound excitons in monolayer MoS$_2$

To further investigate the evolution of defect states induced by the proposed oxygen-incorporated defect-healing process, PL spectroscopy measurements are carried out at low temperature. The temperature-dependent PL measurements for the three types of MoS$_2$ sample are summarized in Supplementary Fig. 22, and the temperature dependence of the observed free-exciton emissions is in accordance with previous studies[34,48]. At lower temperatures (<160 K), besides the free-exciton emissions located at around 1.95 eV, additional PL emission peaks emerge at lower photon

energies (from 1.65 to 1.85 eV). These PL emission peaks have been widely observed in previous studies on MoS$_2$ produced by either mechanical exfoliation or CVD growth and treated with or without O$_2$ plasma[34,60]. Sublinear power dependence of these low-energy PL emission peaks at 77 K is observed (Supplementary Fig. 23), which is in accordance with previous studies[34]. We, thus, attribute the low-energy PL emissions to the radiative recombination of excitons bound to localized defect states. By fitting the power dependent bound-exciton PL emissions with a power law, that is, $I_{PL} \approx P^{\alpha}$, where P is the incident light power, we notice that the power factor α for O-MoS$_2$ and SM-MoS$_2$ samples are 0.72 and 0.88, respectively (Supplementary Fig. 23c). Such a discrepancy in α suggests that the bound exciton states in O-MoS$_2$ and SM-MoS$_2$ may originate from different defect states.

To gather more information about the exciton states in MoS$_2$, we take gate-dependent PL measurements. The PL spectra of O-MoS$_2$,
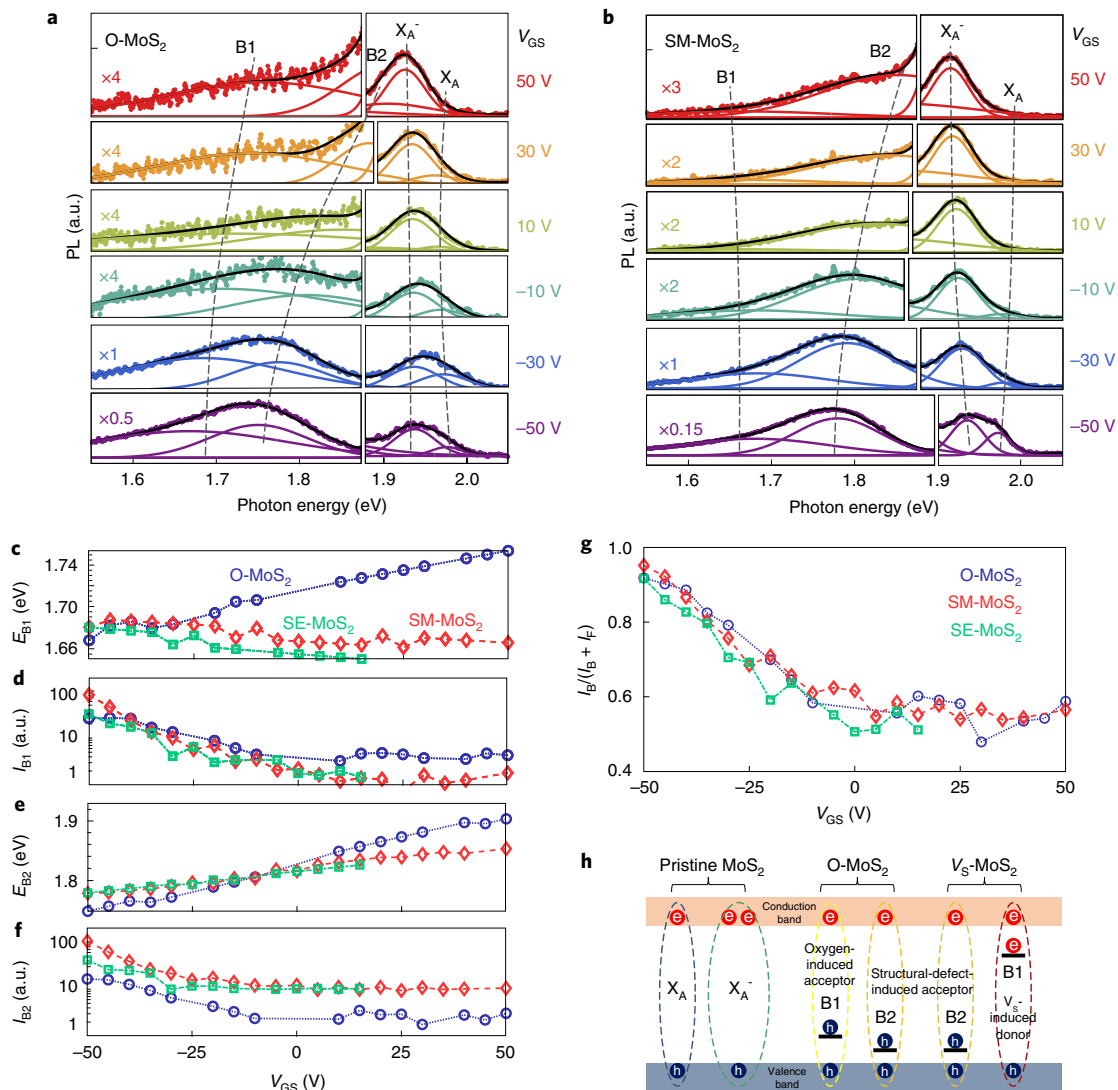
Fig. 5 | Gate-dependent PL at 78 K. a,b, PL spectra of O-MoS$_2$ (**a**) and SM-MoS$_2$ (**b**) at 78 K with different gate voltages (V_{GS}). Each spectrum is fitted with four Gaussian peaks, denoted as B1, B2, X$_A$ and X$_A^-$. **c–f**, Peak positions E_{B1} (**c**) and E_{B2} (**e**) and accumulated intensities I_{B1} (**d**) and I_{B2} (**f**) of the B1 and B2 bound exciton states as a function of V_{GS}. The parameters for O-MoS$_2$, SM-MoS$_2$ and SE-MoS$_2$ are plotted as blue circles, red diamonds and green squares, respectively. **g**, Percentage of bound-exciton-associated accumulative PL intensity ($I_B/(I_B+I_F)$) as a function of V_{GS}. **h**, Diagram of free and bound excitons probed in monolayer MoS$_2$. e, electron; h, hole.

SM-MoS$_2$ and SE-MoS$_2$ with different gate voltages (V_{GS}) are shown in Fig. 5a,b and Supplementary Fig. 24a–c. The free-exciton PL emission at higher photon energies (from 1.85 to 2.00 eV) can be fitted with two Gaussian functions, denoted as X$_A^-$ and X$_A$. The bound-exciton PL emission at lower energies (from 1.65 to 1.85 eV) can be fit with two additional Gaussian functions, denoted as B1 and B2. The gate-dependent peak energies and peak intensities for the negatively charged excitons (or trions, X$_A^-$) and neutral excitons (X$_A$) for the three different types of MoS$_2$ sample are plotted in Supplementary Fig. 24d–h, which are in good agreement with previous studies. More importantly, it is also observed that both peak energies and peak intensities of the B1 and B2 bound exciton emissions vary with gate voltage (Fig. 5c–f).

The trends in exciton peak energy and intensity can be summarized for the three flake types. The peak intensities of both B1 and B2 bound exciton emissions decrease with increasing V_{GS} for all three types of MoS$_2$ samples. This trend is more evident if we plot $I_B/(I_B+I_F)$ as a function of V_{GS} (Fig. 5g), where I_B and I_F are the accumulated PL intensities for bound excitons (B1 and B2) and

free excitons (X$_A^-$ and X$_A$), respectively. The intensity drop can be understood by considering the free-carrier screening of the charged impurity in MoS$_2$. The probability of bound exciton formation is determined by the Debye length of ionized impurity scattering[61] that is screened by the carriers in MoS$_2$, given by $L_D = (\kappa_s \varepsilon_0 k_B T / q^2 n_{2D})^{1/2}$, where κ_s is the relative permittivity, ε_0 is the vacuum permittivity, k_B is the Boltzmann constant, T is the temperature and q is the elementary charge. Evidently, L_D is negatively correlated with electron density due to screening of the Coulomb potential around the charged impurity, which, in turn, influences the population of bound excitons.

The peak energies of B1 and B2 emissions are also tuned by V_{GS}. Specifically, when the gate voltage increases, there is a redshift in the B1 peak in the SM- and SE-MoS$_2$ samples, whereas the B1 peak in the O-MoS$_2$ sample undergoes a blueshift. Meanwhile, a blueshift is observed in the B2 peak in all the three types of sample. These shifts in peak positions can be explained by the exciton recoil effects[15,48,62]. For a charged exciton (defect-bound exciton), since there is an additional electron or hole, the dissociation of these quasiparticles must

accompany an emission of this extra carrier, which consumes extra energy depending on the Fermi level. The directions of shifts in the peak position are opposite for a negatively charged exciton (donor bound) and for a positively charged exciton (acceptor bound). We, thus, identify the B1 state in the O-MoS$_2$ sample and the B2 state in all the three types of sample as acceptor-bound exciton states; further, the B1 state in the SM- and SE-MoS$_2$ samples is a donor-bound exciton state. The disappearance of the donor-bound exciton state and the emergence of a new acceptor state happen simultaneously as oxygen is incorporated into the MoS$_2$ lattices (Fig. 5h).

The LDOS values have shown that the presence of V$_S$ generates defect states below the CBM of MoS$_2$ (Fig. 3b), whereas they are successfully eliminated in O-MoS$_2$ (Fig. 3c,d). Accordingly, these defect states can be associated with the donor-bound exciton state that is only observed in the SM-MoS$_2$ and SE-MoS$_2$ samples. On the other hand, the absence of the donor-bound exciton state in O-MoS$_2$ again evidences that such donor defect states have been effectively healed. Note that both defective and oxygen-incorporated MoS$_2$ exhibit native acceptor-like states close to the valence band minimum (VBM) (Fig. 3b–d and Supplementary Fig. 10), which may be the origin of the B2 acceptor-bound exciton state observed in all three types of MoS$_2$. Because the emergence of an additional acceptor-bound state (B1) takes place only in O-MoS$_2$, but not in SM-MoS$_2$ or SE-MoS$_2$, we speculate that B1 is likely to be associated with the acceptor states that are partially contributed by the O orbitals near the VBM (Fig. 3d). Another important observation is that there are additional O-orbital-contributed states near both CBM and VBM. These shallow defect states behave like effective donors and acceptors, respectively, and thus are mostly complementary to each other. This may be the reason why only less n-type doping—rather than p-type doping—is achieved for O-MoS$_2$ samples, as shown in Fig. 4.

Conclusions

We have reported an O$_2$-CVD technique for fabricating monolayer MoS$_2$ that passivates V$_S$ and suppresses the formation of detrimental donor states. Raman, PL and XPS measurements demonstrate the presence of Mo–O bonds and the resulting electron depletion effect in MoS$_2$. The as-grown O-MoS$_2$ crystals, in comparison to typical CVD MoS$_2$, exhibit a higher work function (5.45 eV) and enhanced PL intensity. Oxygen incorporation also lowers the SBH (<40 meV) and consequently results in a low R_C (1 kΩ μm) at the metal/semiconductor heterojunction. These features are desirable for the development of high-performance MoS$_2$ transistors through O$_2$-CVD and other defect engineering approaches. The defect-healing process based on a one-step CVD strategy could also potentially open a route to modulate the electronic and optoelectronic properties of other 2D TMDs, in an approach that should be scalable and compatible with complementary metal–oxide–semiconductor processes.

Data availability

The data that support the findings within this paper are available from the corresponding author upon reasonable request.

References

1. Erwin, S. C. et al. Doping semiconductor nanocrystals. *Nature* **436**, 91–94 (2005).
2. Chen, B. et al. Highly emissive and color-tunable CuInS$_2$-based colloidal semiconductor nanocrystals: off-stoichiometry effects and improved electroluminescence performance. *Adv. Funct. Mater.* **22**, 2081–2088 (2012).
3. Nowotny, M. K., Sheppard, L. R., Bak, T. & Nowotny, J. Defect chemistry of titanium dioxide. Application of defect engineering in processing of TiO$_2$-based photocatalysts. *J. Phys. Chem. C* **112**, 5275–5300 (2008).
4. Ambacher, O. et al. Two-dimensional electron gases induced by spontaneous and piezoelectric polarization charges in N- and Ga-face AlGaN/GaN heterostructures. *J. Appl. Phys.* **85**, 3222–3233 (1999).
5. Chhowalla, M., Jena, D. & Zhang, H. Two-dimensional semiconductors for transistors. *Nat. Rev. Mater.* **1**, 16052 (2016).
6. Schmidt, H., Giustiniano, F. & Eda, G. Electronic transport properties of transition metal dichalcogenide field-effect devices: surface and interface effects. *Chem. Soc. Rev.* **44**, 7715–7736 (2015).
7. Schmidt, H. et al. Transport properties of monolayer MoS$_2$ grown by chemical vapor deposition. *Nano Lett.* **14**, 1909–1913 (2014).
8. Yuan, S., Roldán, R., Katsnelson, M. & Guinea, F. Effect of point defects on the optical and transport properties of MoS$_2$ and WS$_2$. *Phys. Rev. B* **90**, 041402 (2014).
9. Ge, Y., Wan, W., Feng, W., Xiao, D. & Yao, Y. Effect of doping and strain modulations on electron transport in monolayer MoS$_2$. *Phys. Rev. B* **90**, 035414 (2014).
10. Chae, W. H., Cain, J. D., Hanson, E. D., Murthy, A. A. & Dravid, V. P. Substrate-induced strain and charge doping in CVD-grown monolayer MoS$_2$. *Appl. Phys. Lett.* **111**, 143106 (2017).
11. Vancsó, P. et al. The intrinsic defect structure of exfoliated MoS$_2$ single layers revealed by scanning tunneling microscopy. *Sci. Rep.* **6**, 29726 (2016).
12. Zhou, W. et al. Intrinsic structural defects in monolayer molybdenum disulfide. *Nano Lett.* **13**, 2615–2622 (2013).
13. Hong, J. et al. Exploring atomic defects in molybdenum disulphide monolayers. *Nat. Commun.* **6**, 6293 (2015).
14. Guo, Y., Liu, D. & Robertson, J. Chalcogen vacancies in monolayer transition metal dichalcogenides and Fermi level pinning at contacts. *Appl. Phys. Lett.* **106**, 173106 (2015).
15. Shang, J. et al. Revealing electronic nature of broad bound exciton bands in two-dimensional semiconducting WS$_2$ and MoS$_2$. *Phys. Rev. Mater.* **1**, 074001 (2017).
16. Amani, M. et al. Near-unity photoluminescence quantum yield in MoS$_2$. *Science* **350**, 1065–1068 (2015).
17. Lien, D.-H. et al. Electrical suppression of all nonradiative recombination pathways in monolayer semiconductors. *Science* **364**, 468–471 (2019).
18. Cho, K. et al. Electrical and optical characterization of MoS$_2$ with sulfur vacancy passivation by treatment with alkanethiol molecules. *ACS Nano* **9**, 8044–8053 (2015).
19. Mouri, S., Miyauchi, Y. & Matsuda, K. Tunable photoluminescence of monolayer MoS$_2$ via chemical doping. *Nano Lett.* **13**, 5944–5948 (2013).
20. McDonnell, S., Addou, R., Buie, C., Wallace, R. M. & Hinkle, C. L. Defect-dominated doping and contact resistance in MoS$_2$. *ACS Nano* **8**, 2880–2888 (2014).
21. Schulman, D. S., Arnold, A. J. & Das, S. Contact engineering for 2D materials and devices. *Chem. Soc. Rev.* **47**, 3037–3058 (2018).
22. Kim, C. et al. Fermi level pinning at electrical metal contacts of monolayer molybdenum dichalcogenides. *ACS Nano* **11**, 1588–1596 (2017).
23. Kim, G.-S. et al. Schottky barrier height engineering for electrical contacts of multilayered MoS$_2$ transistors with reduction of metal-induced gap states. *ACS Nano* **12**, 6292–6300 (2018).
24. Wang, J. et al. High mobility MoS$_2$ transistor with low Schottky barrier contact by using atomic thick h-BN as a tunneling layer. *Adv. Mater.* **28**, 8302–8308 (2016).
25. Liu, Y. et al. Approaching the Schottky–Mott limit in van der Waals metal–semiconductor junctions. *Nature* **557**, 696–700 (2018).
26. Wang, Y. et al. Van der Waals contacts between three-dimensional metals and two-dimensional semiconductors. *Nature* **568**, 70–74 (2019).
27. Chee, S. S. et al. Lowering the Schottky barrier height by graphene/Ag electrodes for high-mobility MoS$_2$ field-effect transistors. *Adv. Mater.* **31**, 1804422 (2019).
28. Yu, Z. et al. Towards intrinsic charge transport in monolayer molybdenum disulfide by defect and interface engineering. *Nat. Commun.* **5**, 5290 (2014).
29. Tongay, S. et al. Broad-range modulation of light emission in two-dimensional semiconductors by molecular physisorption gating. *Nano Lett.* **13**, 2831–2836 (2013).
30. Nan, H. et al. Strong photoluminescence enhancement of MoS$_2$ through defect engineering and oxygen bonding. *ACS Nano* **8**, 5738–5745 (2014).
31. Leong, W. S. et al. Tuning the threshold voltage of MoS$_2$ field-effect transistors via surface treatment. *Nanoscale* **7**, 10823–10831 (2015).
32. Lu, J. et al. Atomic healing of defects in transition metal dichalcogenides. *Nano Lett.* **15**, 3524–3532 (2015).
33. Islam, M. R. et al. Tuning the electrical property via defect engineering of single layer MoS$_2$ by oxygen plasma. *Nanoscale* **6**, 10033–10039 (2014).
34. Tongay, S. et al. Defects activated photoluminescence in two-dimensional semiconductors: interplay between bound, charged and free excitons. *Sci. Rep* **3**, 2657 (2013).
35. Kim, M. S. et al. Photoluminescence wavelength variation of monolayer MoS$_2$ by oxygen plasma treatment. *Thin Solid Films* **590**, 318–323 (2015).

36. Ling, X. et al. Role of the seeding promoter in MoS_2 growth by chemical vapor deposition. *Nano Lett.* **14**, 464–472 (2014).

37. Wang, S. et al. Shape evolution of monolayer MoS_2 crystals grown by chemical vapor deposition. *Chem. Mater.* **26**, 6371–6379 (2014).

38. Dumcenco, D. et al. Large-area epitaxial monolayer MoS_2. *ACS Nano* **9**, 4611–4620 (2015).

39. Van Der Zande, A. M. et al. Grains and grain boundaries in highly crystalline monolayer molybdenum disulphide. *Nat. Mater.* **12**, 554–561 (2013).

40. Liu, Z. et al. Strain and structure heterogeneity in MoS_2 atomic layers grown by chemical vapour deposition. *Nat. Commun.* **5**, 5246 (2014).

41. Smithe, K. K., English, C. D., Suryavanshi, S. V. & Pop, E. Intrinsic electrical transport and performance projections of synthetic monolayer MoS_2 devices. *2D Mater.* **4**, 011009 (2016).

42. Chen, W. et al. Oxygen-assisted chemical vapor deposition growth of large single-crystal and high-quality monolayer MoS_2. *J. Am. Chem. Soc.* **137**, 15632–15635 (2015).

43. Cao, D., Shen, T., Liang, P., Chen, X. & Shu, H. Role of chemical potential in flake shape and edge properties of monolayer MoS_2. *J. Phys. Chem. C* **119**, 4294–4301 (2015).

44. Gao, Y., Goodman, A. J., Shen, P.-C., Kong, J. & Tisdale, W. A. Phase-modulated degenerate parametric amplification microscopy. *Nano Lett.* **18**, 5001–5006 (2018).

45. Ponce-Mosso, M. et al. Enhanced photocatalytic activity of amorphous MoO_3 thin films deposited by rf reactive magnetron sputtering. *Catal. Today* **349**, 150–158 (2018).

46. Khademi, A., Azimirad, R., Zavarian, A. A. & Moshfegh, A. Z. Growth and field emission study of molybdenum oxide nanostars. *J. Phys. Chem. C* **113**, 19298–19304 (2009).

47. Diaz, H. C., Addou, R. & Batzill, M. Interface properties of CVD grown graphene transferred onto MoS_2(0001). *Nanoscale* **6**, 1071–1078 (2014).

48. Mak, K. F. et al. Tightly bound trions in monolayer MoS_2. *Nat. Mater.* **12**, 207–211 (2013).

49. Michail, A., Delikoukos, N., Parthenios, J., Galiotis, C. & Papagelis, K. Optical detection of strain and doping inhomogeneities in single layer MoS_2. *Appl. Phys. Lett.* **108**, 173102 (2016).

50. Rice, C. et al. Raman-scattering measurements and first-principles calculations of strain-induced phonon shifts in monolayer MoS_2. *Phys. Rev. B* **87**, 081307 (2013).

51. Chakraborty, B. et al. Symmetry-dependent phonon renormalization in monolayer MoS_2 transistor. *Phys. Rev. B* **85**, 161403 (2012).

52. Kim, J. H. et al. Work function variation of MoS_2 atomic layers grown with chemical vapor deposition: the effects of thickness and the adsorption of water/oxygen molecules. *Appl. Phys. Lett.* **106**, 251606 (2015).

53. Lee, S. Y. et al. Large work function modulation of monolayer MoS_2 by ambient gases. *ACS Nano* **10**, 6100–6107 (2016).

54. Tung, R. T. The physics and chemistry of the Schottky barrier height. *Appl. Phys. Rev.* **1**, 011304 (2014).

55. Huang, L. et al. Role of defects in enhanced Fermi level pinning at interfaces between metals and transition metal dichalcogenides. *Phys. Rev. B* **96**, 205303 (2017).

56. Bampoulis, P. et al. Defect dominated charge transport and Fermi level pinning in MoS_2/metal contacts. *ACS Appl. Mater. Interfaces* **9**, 19278–19286 (2017).

57. English, C. D., Shine, G., Dorgan, V. E., Saraswat, K. C. & Pop, E. Improved contacts to MoS_2 transistors by ultra-high vacuum metal deposition. *Nano Lett.* **16**, 3824–3830 (2016).

58. Smets, Q. et al. Ultra-scaled MOCVD MoS_2 MOSFETs with 42nm contact pitch and 250μA/μm drain current. In *2019 IEEE International Electron Devices Meeting (IEDM)* 23.22.21–23.22.24 (IEEE, 2019).

59. Cui, X. et al. Low-temperature ohmic contact to monolayer MoS_2 by van der Waals bonded Co/h-BN electrodes. *Nano Lett* **17**, 4781–4786 (2017).

60. Goodman, A. J., Willard, A. P. & Tisdale, W. A. Exciton trapping is responsible for the long apparent lifetime in acid-treated MoS_2. *Phys. Rev. B* **96**, 121404 (2017).

61. Lundstrom, M. *Fundamentals of Carrier Transport* (Cambridge Univ. Press, 2009).

62. Zhang, Q. et al. Recoil effect and photoemission splitting of trions in monolayer MoS_2. *ACS Nano* **11**, 10808–10815 (2017).

63. van Dal, M. J. H. et al. Highly manufacturable finFETs with sub-10nm fin width and high aspect ratio fabricated with immersion lithography. In *2007 IEEE Symposium on VLSI Technology* 110–111 (IEEE, 2017).

Author contributions

P.-C.S., Y.L. and J.K. conceived and designed the experiments. P.-C.S. performed the MoS_2 growth and characterization supervised by J.K. P.-C.S. and Y.L. carried out the device fabrication and characterization supervised by T.P. Y.L., P.-C.S. and X.W. performed the low-temperature optical measurements supervised by X.L. C.M. carried out the EFM measurements and interpreted the data supervised by K.E.A. A.-Y.L. performed the doping and strain characterization and analysed the Raman and XPS data. C.S. performed the TEM measurement supervised by J.L. C.S. and X.J. conducted the DFT calculations supervised by J.L. and Y.W. H.W. performed the XPS measurement. N.M. conducted the second-harmonic generation study supervised by W.T. Y.G. and X.J. assisted with further O-MoS_2 synthesis. P.-C.S., Y.L. and J.K. co-wrote the paper. All the authors regularly discussed the results and commented on the manuscript.

Competing interests

The authors declare no competing interests.

Additional information

Supplementary information The online version contains supplementary material available at https://doi.org/10.1038/s41928-021-00685-8.

Correspondence and requests for materials should be addressed to Jing Kong.

Peer review information *Nature Electronics* thanks the anonymous reviewers for their contribution to the peer review of this work.

Reprints and permissions information is available at www.nature.com/reprints.

Publisher's note Springer Nature remains neutral with regard to jurisdictional claims in published maps and institutional affiliations.